

1 **Sparsity Constrained Split Feasibility for**
2 **Dose-Volume Constraints in Inverse Planning**
3 **of Intensity-Modulated Photon or Proton**
4 **Therapy**

5 Scott Penfold^{1,2*}, Rafał Zalas^{3†}, Margherita Casiraghi⁴
6 Mark Brooke², Yair Censor⁵, Reinhard Schulte⁶

¹Department of Medical Physics, Royal Adelaide Hospital
Adelaide, SA 5000, Australia

²Department of Physics,
University of Adelaide, Adelaide, SA 5005, Australia

³Department of Mathematics, The Technion, Technion City,
Haifa 32000, Israel

⁴Paul Scherrer Institute, Center for Proton Therapy (CPT)
Switzerland

⁵Department of Mathematics, University of Haifa
Mt. Carmel, Haifa 3498838, Israel

⁶Department of Basic Sciences, School of Medicine
Loma Linda University, Loma Linda, CA 92354, USA.

(scott.penfold@sa.gov.au)

7 July 10, 2016; Revised January 10, 2017

*†The contributions of the first two authors to this work are of equal shares.

8 **Abstract**

9 A split feasibility formulation for the inverse problem of intensity-modulated radiation
10 therapy (IMRT) treatment planning with dose-volume constraints (DVCs) included in
11 the planning algorithm is presented. It involves a new type of sparsity constraint that
12 enables the inclusion of a percentage-violation constraint in the model problem and
13 its handling by continuous (as opposed to integer) methods. We propose an iterative
14 algorithmic framework for solving such a problem by applying the feasibility-seeking
15 *CQ*-algorithm of Byrne combined with the automatic relaxation method (ARM) that
16 uses cyclic projections. Detailed implementation instructions are furnished. Function-
17 ality of the algorithm was demonstrated through the creation of an intensity-modulated
18 proton therapy plan for a simple 2D C-shaped geometry and also for a realistic base-
19 of-skull chordoma treatment site. Monte Carlo simulations of proton pencil beams
20 of varying energy were conducted to obtain dose distributions for the 2D test case.
21 A research release of the *Pinnacle*³ proton treatment planning system was used to
22 extract pencil beam doses for a clinical base-of-skull chordoma case. In both cases
23 the beamlet doses were calculated to satisfy dose-volume constraints according to our
24 new algorithm. Examination of the dose-volume histograms following inverse planning
25 with our algorithm demonstrated that it performed as intended. The application of our
26 proposed algorithm to dose-volume constraint inverse planning was successfully demon-
27 strated. Comparison with optimized dose distributions from the research release of the
28 *Pinnacle*³ treatment planning system showed the algorithm could achieve equivalent
29 or superior results.

30 **Keywords:** dose-volume constraints, intensity-modulated radiation therapy, sparsity con-
31 straints, split feasibility, the *CQ*-algorithm, inverse planning, automatic relaxation method.

1 Introduction

Intensity-modulated radiation therapy (IMRT) with photons or intensity-modulated proton therapy (IMPT) are rapidly evolving techniques for planning and delivering radiation therapy to solid tumors. For many tumor sites, IMRT with photons has superseded standard radiation therapy (RT) techniques and is becoming the new standard in RT delivery [1, 2, 3, 4, 5]. At existing proton centers, IMPT in combination with active pencil beam scanning is increasingly being used, replacing older passively scattered and collimated proton therapy techniques as a means for more accurately delivering high doses to the target volume and sparing of organs at risk (OARs) as indicated by dosimetric studies [6, 7, 8, 9, 10].

Instead of using a single upper dose bound for OARs and single lower dose bound for the target volumes, it has become a common practice in clinical trials and off-trial photon IMRT treatments to specify more than one dose-volume constraint (DVC), allowing a certain percentage of volume to violate to a certain extent a given bound. This additional DVC, which could be single or multiple, rely on accumulated clinical experience with conformal RT techniques. For example, Gulliford et al. [11] performed a detailed dose-volume analysis of the incidence of clinically relevant late rectal toxicities in patients treated with high-dose photon IMRT for prostate cancer and found that the incidence of moderate-to-severe rectal toxicity for any of six late-toxicity endpoints decreased incrementally for patients whose treatment plans met increasing numbers of DVCs from the set of $V_{30} \leq 80\%$, $V_{40} \leq 65\%$, $V_{50} \leq 55\%$, $V_{60} \leq 40\%$, $V_{65} \leq 30\%$, $V_{70} \leq 15\%$, and $V_{75} \leq 3\%$. Here, $V_X \leq Y$ corresponds to a dose-volume constraint that $Y\%$ of the volume cannot receive more than X Gy. These and similar DVCs for OARs have found their way into clinical trial protocols and practice guidelines over the years, see, e.g., [12].

Most modern inverse planning algorithms attempt to incorporate DVCs by defining sub-volumes with different dose objectives applied to each sub-volume. The multiple objectives are then combined into a single cost function to be minimized. Minimization in RT inverse planning with DVCs has been performed with a number of different approaches. Spirou and

59 Chui [13, Section F] used gradient descent to seek a vector of ray intensities that minimized a
60 cost function representing the sum of all dose constraints violations. However, incorporating
61 DVCs directly into the cost function of the minimization process often renders the objec-
62 tive function non-convex and non-differentiable. This has the disadvantage of potentially
63 resulting in local minima and thereby sub-optimal treatment plans. Cho *et al.* [14] used
64 a similar concept but applied simulated annealing for minimization. Simulated annealing is
65 less susceptible to non-convexity and non-differentiability but is less computationally efficient
66 than gradient descent. Romeijn *et al.* [15, 16] adopted a linear programming approach to
67 handle what they called partial-volume constraints. However to make the problem tractable
68 for computation, they replaced the familiar concept of DVCs by a closely related, but not
69 identical notion of conditional value-at-risk (C-VaR). Zhang and Merritt [17] proposed a new
70 least-squares model to handle DVCs while retaining differentiability at the expense of having
71 to deal with a nested double minimization problem. Therefore, an inverse planning algorithm
72 for DVCs that is computationally efficient, robust to non-convexity and non-differentiability
73 yet without simplifying the problem statement has yet to be developed.

74 In the current work, feasibility-seeking methods, as opposed to minimization algorithms,
75 are applied to RT inverse planning with DVCs. Within the proposed feasibility-seeking
76 approach issues of convexity and differentiability of the cost function do not arise at all
77 because no cost function is used. While the DVCs do require a constraint that is not convex
78 (the sparsity-norm constraint set), we are able to incorporate it into the projection method
79 that we use to solve the feasibility-seeking problem. This is possible because we have devised
80 a way to calculate the projection onto this set in spite of it being non-convex.

81 Another general advantage of the feasibility-seeking approach has to do with the availabil-
82 ity of a class of highly efficacious feasibility-seeking *projection methods*. These methods refer
83 to iterative algorithms that use projections onto sets while relying on the general principle
84 that when a family of, usually closed and convex, constraints sets is present, then projections
85 onto the individual sets are easier to perform than projections onto other sets (intersections,

86 image sets under some transformation, etc.) that are derived from the individual sets. Fur-
87 thermore, projection methods may have algorithmic structures that are particularly suited for
88 parallel computing, such as block-iterative projections (BIP) or string-averaging projections
89 (SAP). They also demonstrate desirable convergence properties and good initial behavior
90 patterns. See, for example, the 1996 review [18], the recent annotated bibliography of books
91 and reviews [19] and its references, and [20].

92 We recently showed that IMPT inverse planning is possible with a fully-discretized,
93 feasibility-seeking approach by iteratively projecting solution vectors in the beam intensity
94 vector space onto half-spaces representing dose constraints in target and OAR volumes [21].
95 In our preliminary work, we demonstrated that with these iterative projection algorithms,
96 feasible solutions meeting the planning objectives can be found that meet target and nor-
97 mal tissues dose bounds, in particular, if the constraints are not too challenging and/or the
98 treatment modality is very conformal (e.g., by using protons).

99 In this paper, we use the fully-discretized feasibility-seeking approach applicable to either
100 photon IMRT or IMPT inverse planning which leads to a mathematical feasibility problem.
101 The upper and lower bounds on the doses to the various structures define the linear inequal-
102 ity constraints of the feasibility problem, which is solved by feasibility-seeking projection
103 methods without attempting to minimize any cost function. Within this setup, we propose
104 and investigate a novel method for allowing the feasibility-seeking inverse planning algorithm
105 to automatically account for DVCs.

106 In the next section, we rigorously define the notion of percentage-violation constraint
107 (PVC), which does not seem to have been used in the mathematical optimization community
108 until now. A PVC injects integers into the problem which makes it difficult to solve. To
109 circumvent this difficulty, we reformulate the PVC with the aid of a sparsity norm that counts
110 the number of non-zero entries in a vector. This enables us to replace the original feasibility
111 problem with PVC by another feasibility problem that includes non-convex constraints for
112 the sparsity norm. For the resulting feasibility problem with this non-convex sparsity norm

113 induced constraint we develop a new iterative projection algorithm which is a combination
 114 of the CQ -algorithm [22] and the automatic relaxation method (ARM) [23].

115 2 Methods

116 2.1 Linear feasibility with percentage-violation constraints

117 Given p closed convex subsets $Q_1, Q_2, \dots, Q_p \subseteq R^n$ of the n -dimensional Euclidean space
 118 R^n , expressed as level sets

$$Q_j = \{x \in R^n \mid f_j(x) \leq v_j\}, \text{ for all } j \in J := \{1, 2, \dots, p\}, \quad (1)$$

119 where $f_j : R^n \rightarrow R$ are convex functions and v_j are some given real numbers, the convex
 120 feasibility problem (CFP) is to find a point $x^* \in Q := \bigcap_{j \in J} Q_j$. If $Q = \emptyset$ where \emptyset is the empty
 121 set then the CFP is said to be inconsistent.

122 Denoting the inner product of two vectors in R^n by $\langle a, b \rangle := \sum_{i=1}^n a_i b_i$, we consider the
 123 following linear feasibility problem (LFP) with percentage-violation constraint (PVC).

124 **Problem 1 *Linear Feasibility with Percentage-Violation Constraint (PVC).*** *Given*
 125 *a CFP as in (1) with $f_j(x) = \langle a^j, x \rangle$ and two real numbers $0 \leq \alpha \leq 1$ and $0 < \beta < 1$, find a*
 126 *vector x^* that solves the system*

$$\langle a^j, x \rangle \leq v_j, \text{ for all } j \in J \quad (2)$$

subject to the additional PVC constraint that:

**In up to a fraction α (i.e., $100\alpha\%$) of the total number of inequalities
 in (2) the right-hand side bounds v_j may be potentially violated
 by up to a fraction β (i.e., $100\beta\%$) of their values.** (3)

127 A PVC is an integer constraint by its nature. It changes the CFP to which it is attached
 128 from being a continuous feasibility problem into becoming a mixed integer feasibility problem.
 129 In the field of intensity-modulated radiation therapy (IMRT) treatment planning dose-volume
 130 constraints (DVCs) are traditionally used to evaluate treatment plans. DVCs are percentage-
 131 violation constraints but without properly incorporating them into the algorithm itself it is
 132 not possible to a priori guarantee that a solution will indeed obey them.

133 In this paper we propose a novel way to incorporate PVCs via the notion of a sparsity norm
 134 and derive a tractable model and algorithmic approach, along with detailed implementation
 135 instructions for using it, to solve DVCs feasibility problems for inverse planning in IMRT.

136 2.2 IMRT problem statement

137 We consider the following linear interval feasibility problem (LIFP) which is the basic model
 138 for the inverse problem in the fully-discretized approach to IMRT treatment planning [24,
 139 25, 26]:

Problem 2 *Linear Interval Feasibility: the basic model for the inverse problem in the fully-discretized approach to IMRT treatment planning. Find $x^* \in R^n$ for which the following hold:*

$$0 \leq A_1 x \leq b^1, \tag{4}$$

$$b^3 \geq A_2 x \geq b^2, \tag{5}$$

$$0 \leq A_3 x \leq b^4, \tag{6}$$

$$x \geq 0, \tag{7}$$

140 where $A_1 \in R_+^{m_1 \times n}$, $A_2 \in R_+^{m_2 \times n}$, $A_3 \in R_+^{m_3 \times n}$ are given matrices, $b^1 \in R_+^{m_1}$, $b^2, b^3 \in R_+^{m_2}$,
 141 $b^4 \in R_+^{m_3}$ are given vectors. (The subscript + denotes the nonnegative orthant.)

142 In IMRT the row inequalities of (4) represent voxels of an *organ at risk* (OAR) whose
 143 permitted absorbed doses should not exceed b_t^1 for each voxel t in this structure. The row

144 inequalities of (6) represent voxels of another OAR whose permitted absorbed doses should
 145 not exceed b_t^4 for each voxel t in this structure. The row inequalities of (5) represent voxels
 146 of a *planning target volume* (PTV) whose permitted absorbed doses should be above b_t^2 , but
 147 should not exceed b_t^3 , for each voxel t in this structure.

148 Our tool to “translate” the integer constraint (3) into a “continuous” one is the notion of
 149 sparsity norm, called elsewhere the zero-norm, of a vector $x \in R^n$ which counts the number
 150 of nonzero entries of x , that is,

$$\|x\|_0 := |\{x_i \mid x_i \neq 0\}|, \quad (8)$$

151 where $|\cdot|$ denotes here the cardinality, i.e., the number of elements of a set. This notion has
 152 been recently used for various purposes in compressed sensing, machine learning and more.
 153 The “lower + operation” on a vector $x \in R^n$ means that, for all $i = 1, 2, \dots, n$,

$$(x_+)_i := \max(0, x_i) = \begin{cases} x_i, & \text{if } x_i > 0, \\ 0, & \text{if } x_i \leq 0. \end{cases} \quad (9)$$

154 Obviously, x_+ is always a component-wise nonnegative vector. Hence, $\|x_+\|_0$ counts the
 155 number of positive entries of x and is defined by

$$\|x_+\|_0 := |\{x_i \mid x_i > 0\}|. \quad (10)$$

156 To incorporate a DVC related to (4) into the LIFP of Problem 2 we formulate another
 157 feasibility problem as follows.

Problem 3 *Linear Interval Feasibility with DVC for the inverse problem in the fully-discretized approach to IMRT treatment planning.* Find $x^* \in R^n$ for which

$$0 \leq A_1x \leq (1 + \beta)b^1, \quad (11)$$

$$b^3 \geq A_2x \geq b^2, \quad (12)$$

$$0 \leq A_3x \leq b^4, \quad (13)$$

$$x \geq 0, \quad (14)$$

$$\|(A_1x - b^1)_+\|_0 \leq \alpha m_1, \quad (15)$$

158 where $A_1, A_2, A_3, b^1, b^2, b^3$ and b^4 are as in (4)–(7), and $\beta > 0$ and $\alpha \in [0, 1]$ are given real
159 numbers.

160 In this problem (11) allows the doses to voxels of this structure to “overflow” by β . (13)
161 represents an OAR to which we do not attach a DVC for now. (12) represents a PTV to
162 which we do not attach a DVC for now. (14) are the nonnegativity constraints on the solution
163 vector of intensities.

164 The novelty of the model lies in (15). It says that since we demanded originally $A_1x \leq b^1$
165 in (4) we must look at the “plussed difference vector” $(A_1x - b^1)_+$. It is nonnegative and has
166 a nonzero component exactly and only in components that belong to row inequalities in (11)
167 for which (4) is violated.

168 The zero-norm of $(A_1x - b^1)_+$ is thus equal to the number of those violations and (15)
169 restricts this number to be not greater than αm_1 where m_1 is the total number of row
170 inequalities (i.e., voxels) in the OAR described by (11). Thus, (15) guarantees that the
171 number of violations up to β in (11) remains at bay under the number αm_1 . In the following
172 we propose to use an efficient iterative projections method to solve Problem 3.

2.3 Projection methods for feasibility-seeking

Projections onto sets are used in a wide variety of methods in optimization theory but here *projection methods* refer to iterative algorithms that use projections onto sets while relying on the general principle that when a family of, usually closed and convex, sets is present, then projections onto the given individual sets are easier to perform than projections onto other sets (intersections, image sets under some transformation, etc.) that are derived from the given family of individual sets.

Projection methods may have different algorithmic structures, such as block-iterative projections (BIP) or string-averaging projections (SAP) of which some are particularly suitable for parallel computing, and they demonstrate nice convergence properties and/or good initial convergence patterns. This class of algorithms has witnessed great progress in recent years and its member algorithms have been applied with success to many scientific, technological and mathematical problems. See, e.g., the 1996 review [18], the recent annotated bibliography of books and reviews [19] and its references, the excellent book [27], or [20].

For the LIFP of Problem 3 one can use any of a variety of projection methods to handle linear inequality constraints. The most famous of those might be the Agmon-Motzkin-Schoenberg (AMS) cyclic feasibility-seeking algorithm [28, 29]. In this paper we adopt a projection method of a particular nature, namely, the automatic relaxation method (ARM) for solving interval linear inequalities of [23, Algorithm 1].

ARM has two advantages over other projection methods applicable to this problem: (i) it handles in each iteration an interval constraint and does not need to handle the right-hand side and left-hand side inequalities of an interval separately, (ii) additionally, it automatically implements a relaxation strategy for the projections which takes into account how far from the hyperslab, defined by an interval constraint, is the point that needs to be projected on it and automatically and continuously adjusts the relaxation parameter for the projection accordingly. The ARM generalizes the algebraic reconstruction technique ART3 [30] and is further discussed in Subsection 5.10 of Censor and Zenios [31].

200 **2.4 Algorithmic approach**

201 First we observe that Problem 3 is a split feasibility problem. Split feasibility problems
 202 were introduced first in [32] and further studied in [33, 34] and many other publications.
 203 The constraints (11)–(13) can be collectively described by $c \leq Ax \leq b$, where A is an
 204 $(m_1 + m_2 + m_3) \times n$ matrix composed from blocks

$$A := \begin{pmatrix} A_1 \\ A_2 \\ A_3 \end{pmatrix}, \tag{16}$$

205 b is an $(m_1 + m_2 + m_3)$ vector given by

$$b := \begin{pmatrix} (1 + \beta)b^1 \\ b^3 \\ b^4 \end{pmatrix}, \tag{17}$$

206 and c is an $(m_1 + m_2 + m_3)$ vector given by

$$c := \begin{pmatrix} 0 \\ b^2 \\ 0 \end{pmatrix}, \tag{18}$$

207 and they, along with (14) all reside in the space R^n of intensity vectors x . On the other hand,
 208 the sparsity constraint (15) takes place in the space R^{m_1} where the vectors of doses in the
 209 OAR (4) are, namely, the vector b^1 and the vectors $y = A_1x$. Therefore, we must use not plain
 210 feasibility-seeking methods but feasibility-seeking methods for split feasibility problems.

211 In the space R^n of intensity vectors we define the set

$$C := \{x \in R^n \mid c \leq Ax \leq b\} \cap R_+^n \tag{19}$$

212 where A , b and c are as in (16), (17) and (18), respectively, and R_+^n is the nonnegative orthant
 213 of R^n . In R^{m_1} , the space of dose vectors of the OAR structure represented by (4), we define
 214 the set

$$Q := \{y \in R^{m_1} \mid \|(y - b^1)_+\|_0 \leq \alpha m_1\} \quad (20)$$

215 with b^1 and αm_1 as in (11). If a point $y = A_1 x$ is in Q then it is guaranteed to fulfil (15).
 216 So, our split feasibility problem is to find a point $x^* \in C$ such that $A_1 x^* \in Q$, precisely
 217 describing Problem 3 above.

218 Common feasibility or split feasibility problems deal with convex sets but here we observe
 219 that Q is not a convex set. However, we show below how to project onto it orthogonally,
 220 thus enabling to use a feasibility-seeking projection method for our Problem 3.

221 To solve the split feasibility formulation of Problem 3 we propose to use the CQ -algorithm
 222 [22] for the sets C and Q given by (19) and (20), respectively. It has the advantage that
 223 it does not require to calculate the inverse A_1^{-1} of A_1 in order to “go back” from R^{m_1} to
 224 R^n within the iterative process. Instead, it uses the transposed matrix A_1^T which is readily
 225 available. The CQ -algorithm [22, Algorithm 1.1] is in fact a projected Landweber method
 226 for the split feasibility formulation of Problem 3.

227 In the sequel $P_\Omega(z)$ denotes an orthogonal projection of a vector z onto a set Ω . All data
 228 quantities mentioned below are as in Problem 3. Since Q is not a convex set there might be
 229 more than one point for P_Q in (21) below, therefore, the symbol \in therein means that x^{k+1}
 230 could be any projection point onto Q of the vector in the parentheses whose projection onto
 231 Q is sought after, and can be arbitrarily chosen from those if more than one exists.

232 **Algorithm 4** *The CQ -Algorithm for the Split Linear Feasibility Problem with a*
 233 *DVC.*

234 **Step 0:** Take an arbitrary $x^0 \in R^n$, and set $k = 0$.

235 **Step 1:** For a current iterate x^k calculate $A_1 x^k$ and compute the next iterate by

$$x^{k+1} \in P_C \left(x^k + \gamma A_1^T (P_Q(A_1 x^k) - A_1 x^k) \right). \quad (21)$$

236 If a stopping criterion applies then stop, otherwise go back to the **Step 1** with $k \leftarrow k+1$.

237 Next we explain how to do the projections onto C and onto Q , and how to choose the
 238 parameter γ in (21). Since Q of (20) is not convex, the projection P_Q may be multivalued.
 239 Nevertheless, for any $z \in R^{m_1}$, we can calculate $P_Q(z)$ by using the following formula

$$P_Q(z) = P_{\bar{Q}}(z - b^1) + b^1 \quad (22)$$

240 where

$$\bar{Q} := \{y \in R^{m_1} \mid \|y_+\|_0 \leq \alpha m_1\}. \quad (23)$$

241 Hence the projection of a point $z \in R^{m_1}$ onto the set Q of (20) is obtained by projecting the
 242 shifted point $(z - b^1)$ onto the set \bar{Q} and adding b^1 to the result. The proof of this fact can
 243 be found in the Appendix.

244 Therefore, the problem reduces to computing a projection onto \bar{Q} . This is done according
 245 to the following recipe: First count how many components of $(z - b^1)$ are positive, say ℓ .
 246 Then,

$$P_{\bar{Q}}(z - b^1) = \begin{cases} (z - b^1), & \text{If } \ell \leq \alpha m_1, \\ w, & \text{If } \ell > \alpha m_1, \end{cases} \quad (24)$$

247 where w is the vector obtained from $(z - b^1)$ by replacing its $\ell - \alpha m_1$ smallest positive
 248 components by zeros and leaving the others unchanged. If $\ell \leq \alpha m_1$ then the point $(z - b^1)$
 249 is already inside \bar{Q} , thus $P_{\bar{Q}}(z - b^1) = (z - b^1)$. We will use the above for $z = A_1 x^k$ in (21).

250 Following the seminal CQ -algorithm [22], designed for the case when both sets C and
 251 Q are convex, we propose that the parameter γ in (21) will be user-chosen from the open
 252 interval $0 < \gamma < 2/\theta$ where θ is pre-calculated once. To do so we employ [35, Corollary 2.3]
 253 by using the squared Frobenius matrix norm $\|A_1\|_F^2$ and defining

$$\theta := \|A_1\|_F^2 = \sum_{i=1}^{m_1} \sum_{j=1}^n |a_{ij}|^2, \quad (25)$$

254 where for $i = 1, 2, \dots, m_1$ and $j = 1, 2, \dots, n$, the entries of A_1 are a_{ij} .

255 In the practical implementation we replace the projection onto C (21) by a sequence of
 256 projections onto the individual inequalities of the constraints (11)–(13) that are collectively
 257 described by $c \leq Ax \leq b$ with where A , b and c are as in (16), (17) and (18), respectively,
 258 according to a feasibility-seeking projection method of our choice. All of the above leads to
 259 our proposed Dose-Volume Split-feasibility (DVSF) Algorithm.

260 **Algorithm 5** *The Dose-Volume Split-feasibility (DVSF) Algorithm.*

261

262 **Step (-1):** Read all data from Problem 3 and calculate (once) the transposed matrix A_1^T ,
 263 the value of θ according to (25), and choose a parameter γ in the open interval $0 < \gamma < 2/\theta$.

264 **Step 0:** Take an arbitrary $x^0 \in R_+^n$, and set $k := 0$.

265 **Step 1:** Project A_1x^k onto Q as follows:

266 **Step 1.1:** For the current iterate x^k compute A_1x^k , count the coordinates of $(A_1x^k - b^1)$
 267 that are positive and denote their number by ℓ .

268 **Step 1.2:** Calculate (using (24)) with $z = A_1x^k$

$$v^k := P_Q(A_1x^k - b^1). \quad (26)$$

269 **Step 1.3:** Calculate a projection of A_1x^k onto Q (following (22)–(23)):

$$P_Q(A_1x^k) = v^k + b^1. \quad (27)$$

270 **Step 2:** Calculate $u^k \in R^n$ by the formula

$$u^k = x^k + \gamma A_1^T (P_Q(A_1x^k) - A_1x^k). \quad (28)$$

271 **Step 3:** Instead of projecting u^k onto C as required in (21), use u^k from **Step 2** as
 272 an initial point and perform a sweep (or several sweeps) of a feasibility-seeking projection

273 method for the inequalities of (11)–(14). When stopping this sweep (or several sweeps) take
 274 the resulting vector as the next iterate x^{k+1} .

275 **Step 4:** If a stopping criterion applies then stop, otherwise go back to the **Step 1** with
 276 $k \leftarrow k + 1$.

277 Algorithm 5 is a general scheme that is made specific by choosing a feasibility-seeking
 278 projection method to be used in its **Step 3**. Consult Bauschke and Borwein [18] for a review
 279 of such algorithms, see Censor and Cegielski [19] for an annotated bibliography of books and
 280 reviews on the subject and Censor *et al.* [20] for a review with experimental results.

281 We adopted here the automatic relaxation method (ARM) for feasibility-seeking [23]. We
 282 give a generic description of this algorithm by considering the problem of solving iteratively
 283 large and possibly sparse systems of interval linear inequalities of the form

$$w_j \leq \langle a^j, x \rangle \leq v_j, \quad j = 1, 2, \dots, p, \quad (29)$$

284 where $a^j \in R^n$ are given, for all j , and $w = (w_j) \in R^p$, and $v = (v_j) \in R^p$ are given too.
 285 Assuming that the system is *feasible*, an $x^* \in R^n$ which solves (29) is required. Geometrically,
 286 the system represents p nonempty hyperslabs in R^n , each being the nonempty intersection of
 287 a pair of half-spaces. If we are willing to ignore the slabs structure of the problem it could be
 288 addressed as a system of $2p$ linear one-sided inequalities and solved by the Agmon-Motzkin-
 289 Schoenberg (AMS) algorithm [28, 29]. The ARM takes advantage of the interval structure
 290 of the problem by handling in every iterative step a pair of inequalities and it also realizes a
 291 specific relaxation principle (see [23] for details) in an automatic manner. External relaxation
 292 parameters are available on top of the built-in automatic relaxation principle.

293 For every hyperslab of the system (29) denote by

$$\overline{H}_j := \{x \in R^n \mid \langle a^j, x \rangle = v_j\} \text{ and } \underline{H}_j := \{x \in R^n \mid \langle a^j, x \rangle = w_j\} \quad (30)$$

294 its bounding hyperplanes. The median hyperplane will be

$$H_j := \{x \in R^n \mid \langle a^j, x \rangle = \frac{1}{2}(v_j + w_j)\}, \quad (31)$$

295 and the half-width ψ_j of the hyperslab is

$$\psi_j = \frac{v_j - w_j}{2 \|a^j\|}, \quad (32)$$

296 where $\|\cdot\|$ stands for the Euclidean 2-norm. The signed distance of a point $z \in R^n$ from the
297 j -th median hyperplane H_j is given by

$$d(z, H_j) = \frac{\langle a^j, z \rangle - \frac{1}{2}(v_j + w_j)}{\|a^j\|}. \quad (33)$$

298 Denoting $d_{j(k)} := d(x^k, H_{j(k)})$, the automatic relaxation method is as follows.

299 **Algorithm 6** *The Automatic Relaxation Method (ARM).*

300 **Initialization:** $x^0 \in R^n$ is arbitrary.

301 **Iterative step:** Given a current iterate x^k calculate the next iterate x^{k+1} by

$$x^{k+1} = \begin{cases} x^k, & \text{if } |d_{j(k)}| \leq \psi_{j(k)}, \\ x^k - \frac{\lambda_k}{2} \left(\frac{d_{j(k)}^2 - \psi_{j(k)}^2}{d_{j(k)}} \right) \frac{a^{j(k)}}{\|a^{j(k)}\|}, & \text{otherwise.} \end{cases} \quad (34)$$

302 **Control:** The control sequence $\{j(k)\}_{k=0}^{\infty}$ according to which hyperslabs are picked during
303 iterations is cyclic on $\{1, 2, \dots, m\}$, i.e., $j(k) = k \bmod m + 1$.

304 **Relaxation parameters:** External relaxation parameters $\{\lambda_k\}_{k=0}^{\infty}$, available on top of
305 the built-in automatic relaxation principle are confined, for all $k \geq 0$, to

$$\epsilon_1 \leq \lambda_k \leq 2 - \epsilon_2, \text{ for some user-chosen arbitrarily small } \epsilon_1, \epsilon_2 > 0. \quad (35)$$

306 2.5 Performance Testing

307 Performance tests with two different geometries were carried out to verify the functionality
308 of the proposed algorithmic structure for IMRT. Applications to IMPT are presented in the
309 current work. However, the algorithm is not proton specific, and is equally applicable to any
310 form of IMRT. Only the values of the matrix A differ when different forms of radiation are
311 used.

312 2.5.1 Simplified 2D C-shaped geometry

313 A 2D test geometry was defined to simulate an axial cross-section of a tumour volume sur-
314 rounding an organ at risk. The test geometry is illustrated in Figure 1. Structure pixels were
315 defined with a resolution of 1 mm, also coinciding with the dose grid.

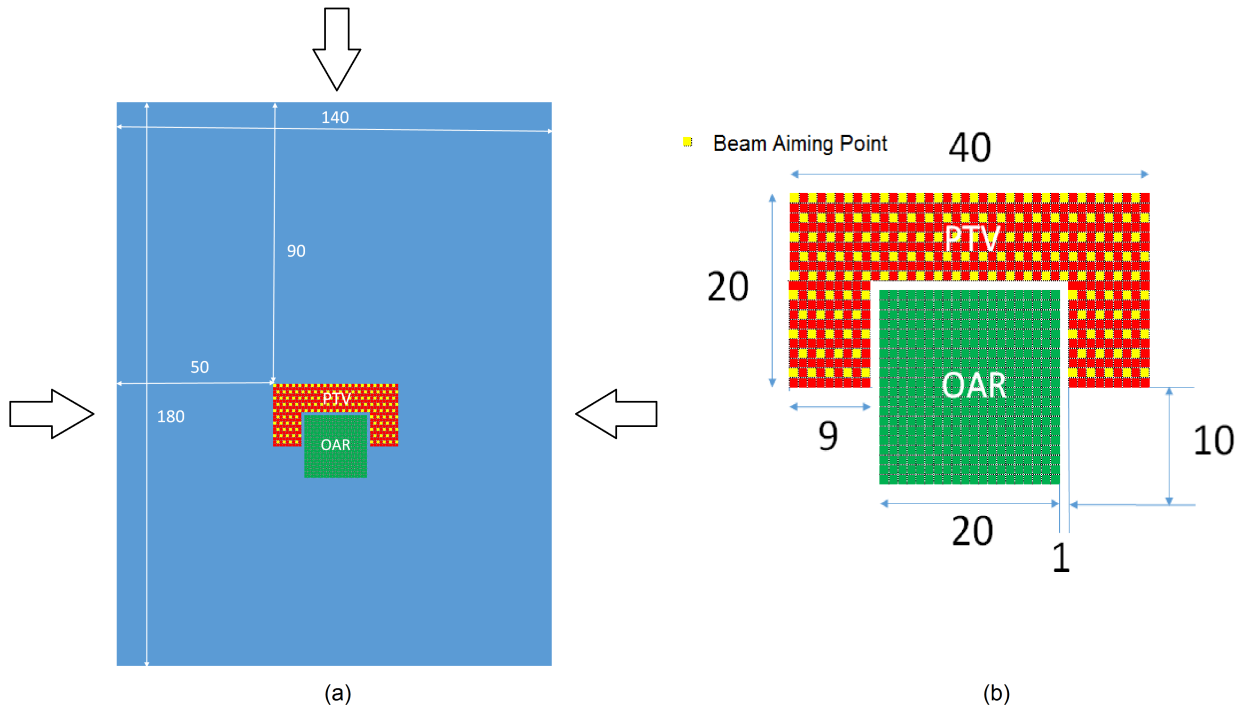


Figure 1: (a) Simplified 2D geometry simulating a tumour surrounding the brainstem. Arrows indicate the proton beam directions selected. (b) Magnified view of the target structure (PTV) and the avoidance structure (OAR). Dimensions are in millimetres. The yellow squares represent locations of delivered Bragg peaks from each beam.

316 A proton pencil beamlet spacing of 2 mm, evenly distributed throughout the PTV struc-
317 ture, was used. Three beam angles were used to deliver dose to the PTV area. Each beam
318 contained 146 proton pencil beamlets. The dose deposited by each pencil beamlet in the dose
319 grid was calculated with the Monte Carlo toolkit Geant4 [36] and recorded in a text file.

320 The simulated beamlets were uniform circular proton beams of 2 mm diameter. A pre-
321 absorber made of 5.5 cm of polyethylene was inserted in the beams at 5 cm in front of the
322 irradiated geometry in order to smooth the Bragg peaks and avoid dose distribution ripples
323 due to beamlet spacing. The beamlet energies for each aiming point were extracted from a
324 calibration curve. The energy used ranged from 118.5 MeV to 153 MeV with a resolution of
325 0.5 MeV. The material of all the structures of the irradiated geometry was assumed to be
326 water.

327 The standard electromagnetic physics (G4EmStandardPhysics) and hadron physics mod-
328 els (G4HadronPhysicsQGSP_BIC_HP) were used for proton tracking. Hadron elastic scat-
329 tering physics, stopping physics, ion physics and decays models were also activated. A range
330 cut of 0.1 mm was set for all particles. For each beamlet, 10^6 events were simulated and the
331 mean absorbed dose per proton was calculated at each pixel of the dose grid.

332 A series of dose-volume constraints (DVCs) were defined to verify the functionality of the
333 algorithm. These included:

- 334 • dose only constraints (DOCs) applied to both the PTV and OAR structures
- 335 • a single DVC associated with a single structure (the OAR structure)
- 336 • multiple (two) DVCs associated with a single structure (the OAR structure)
- 337 • DVCs associated with multiple structures (the PTV structure and the OAR structure)

338 At this point it is instructive to reconcile the dose-volume terminology used in the current
339 work and the terminology commonly used in the literature. Let us consider an example where
340 a prescription has been made to an OAR such that only 20% of the volume can receive more

341 than 40 Gy and none of the volume can receive more than 50 Gy. Using the terminology
 342 of the current work, this would correspond to values of $\alpha = 0.2$, $b_1 = 40$ Gy, and $\beta = 0.25$
 343 in Problem 3. Using the common terminology, this would correspond to $D_{20\%} \leq 40$ Gy and
 344 $D_{max} = 50$ Gy.

345 Table 1 lists the combination of DVCs enforced in the current work, using the common
 346 terminology of IMRT DVCs. The dose prescriptions and percentage volume violations were
 347 chosen to allow for a demonstration of the functionality of the algorithm.

348 The initial pencil beam intensity vector before inverse planning was set to unity. The dose
 349 distribution resulting from the initial intensity vector is shown in Figure 2(a). The proposed
 350 algorithm was run for 2000 cycles for each prescription listed in Table 1. In this terminology,
 351 one cycle corresponds to one complete processing of all DVCs and DOCs applied to each
 352 pixel within both the PTV and OAR structures.

Table 1: Prescriptions associated with PTV and OAR structures in order to test the functionality of the proposed DVSF algorithm (Algorithm 5) in a simplified 2D geometry.

Prescription	OAR	PTV
1	$D_{max} = 45$ Gy	$D_{min} = 70$ Gy $D_{max} = 77$ Gy
2	$D_{15.5\%} \leq 45$ Gy $D_{max} = 70$ Gy	$D_{min} = 70$ Gy $D_{max} = 77$ Gy
3	$D_{50\%} \leq 25$ Gy $D_{15.5\%} \leq 45$ Gy $D_{max} = 70$ Gy	$D_{min} = 70$ Gy $D_{max} = 77$ Gy
4	$D_{8.5\%} \leq 45$ Gy $D_{max} = 70$ Gy	$D_{min} = 66.5$ Gy $D_{95\%} \geq 70$ Gy $D_{max} = 77$ Gy

2.5.2 Clinical 3D geometry

In keeping with the 2D geometry, a base of skull chordoma IMPT treatment plan was chosen due to the challenging constraints imposed by a target structure surrounding an avoidance structure. The *Philips Pinnacle*³ treatment planning system (Philips Healthcare, Koninklijke Philips N.V.) was used to contour the PTV and brainstem. The exported DICOM RT (structure) files were imported into a MATLAB (The MathWorks, Inc.) script and the brainstem and PTV contours were mapped over the CT coordinates. A dose grid was created in MATLAB to match that defined in *Pinnacle*³. The dimensions were $42 \times 43 \times 9$ voxels with resolutions of 2 mm, 2 mm and 3 mm in the x , y and z dimensions, respectively. The dose grid was twice as large as the CT pixel size in the x and y dimension and equivalent to the CT resolution in the z dimension. A reduced number of slices (9) was required due to memory restrictions encountered during the export of pencil beamlet doses.

An IMPT treatment plan was created in the *Pinnacle*³ research release of proton pencil beam scanning (PBS). Two beams were targeted at the PTV from angles of 80° and 280° , containing 574 and 564 beamlets, respectively. A range shifter of 7.5 cm thickness was used with both beams to ensure proximal PTV coverage. Distal and proximal margins for pencil beam placement were automatically calculated as a percentage of proton range. The dose grid resulting from each unit intensity beamlet was exported from *Pinnacle*³. Beamlet parameters were set to 80% layer overlap, a lateral spot resolution of 0.6 cm, a lateral target margin of 0.4 cm and 3 standard deviation dose spread during dose calculation. Dose was calculated with the analytical PBS algorithm which includes nuclear attenuation and an energy and material dependent multiple Coulomb scattering model.

For each structure A -matrices were created by combining the geometry defined by the DICOM RT structures and the dose grid obtained for each beamlet. Each 3D beamlet dose grid was rearranged to a 1D vector which became a column of an A -matrix. Each row of the A_{OAR} matrix corresponded to a voxel of the brainstem and likewise each row of the A_{PTV} matrix corresponded to a voxel of the PTV.

380 Two DVCs were tested for the base of skull chordoma IMPT treatment plan (see Table
 381 2). The DVCs differed in the dose objectives for the brainstem while keeping the PTV
 382 objectives constant. The same DVCs were applied consistently for both the DVSF algorithm
 383 (Algorithm 5) and *Pinnacle*³.

Table 2: Prescriptions associated with PTV and OAR (brainstem) structure for a clinical test case.

Prescription	OAR	PTV
1	$D_{\max} = 54 \text{ Gy}$ $D_{5\%} \leq 50 \text{ Gy}$	$D_{\min} = 66.5 \text{ Gy}$ $D_{\max} = 74.9 \text{ Gy}$ $D_{95\%} \geq 70 \text{ Gy}$
2	$D_{\max} = 40 \text{ Gy}$ $D_{5\%} \leq 35 \text{ Gy}$	$D_{\min} = 66.5 \text{ Gy}$ $D_{\max} = 74.9 \text{ Gy}$ $D_{95\%} \geq 70 \text{ Gy}$

384 Independent values for the parameter γ of (28) were used for the OAR and PTV and
 385 are denoted by γ_{PTV} and γ_{OAR} . These values were determined from the structure-specific
 386 calculation of θ in (25), denoted by θ_{PTV} and θ_{OAR} . The relaxation parameters λ_k of (34)
 387 are fixed throughout the iterations and represented by λ_{PTV} and λ_{OAR} .

388 3 Results

389 3.1 Simplified 2D C-shaped geometry

390 The dose distributions following inverse planning for Prescriptions 1 and 4 in Table 1 are
 391 shown in Figure 2(b) and 2(c). The dose-volume histograms following inverse planning for
 392 all cases listed in Table 1 are presented in Figure 3.

393 The dose distributions (Figure 2) allow for a qualitative assessment of the functionality of
 394 the DVSF algorithm (Algorithm 5). It is evident that the dose resulting from unit intensity

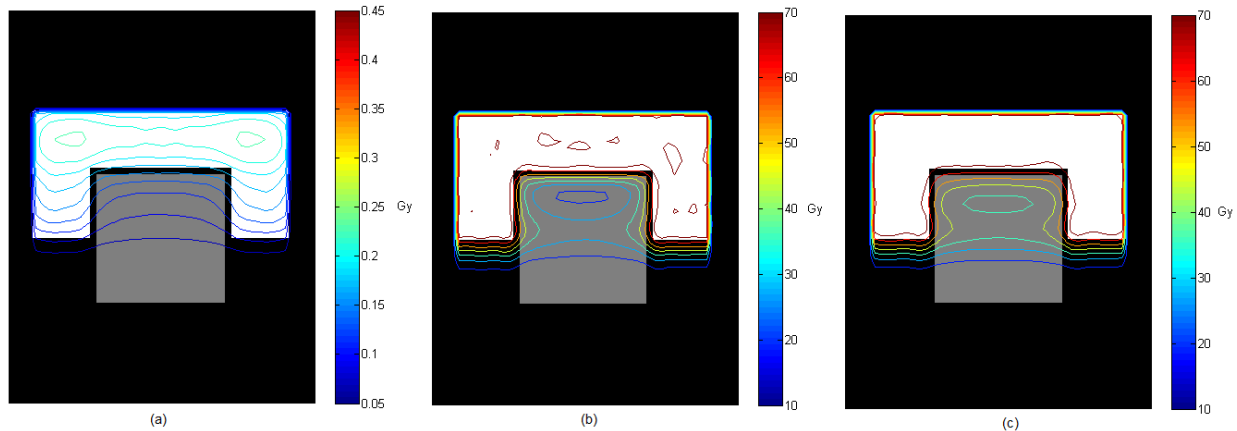


Figure 2: Isodose contours corresponding to (a) unit intensity pencil beams, (b) dose only constraints (Prescription 1), and (c) DVCs applied to both the PTV structure and the OAR structure (Prescription 4).

395 pencil beamlets is successfully modulated toward the desired dose distribution. However, for a
 396 quantitative assessment the dose-volume histograms must be considered. When Prescription
 397 1 DOCs were applied the dose objectives on the PTV structure could not be met (Figure
 398 3(a)). Introducing the DVC on the OAR structure relaxed these conditions and resulted in
 399 satisfaction of the dose objectives on the PTV structure (Figure 3(b)). While the DVC on the
 400 OAR structure was not achieved in Prescription 2, continued iterations would have resulted
 401 in a dose distribution approaching the DVC more closely. The DVSF algorithm (Algorithm
 402 5) was shown to function with multiple DVCs applied to a single structure (Figure 3(c)), and
 403 with DVCs applied to multiple structures (Figure 3(d)).

404 3.2 Clinical 3D geometry

405 Cumulative DVHs for Prescription 1 of Table 2 using the DVSF algorithm (Algorithm 5)
 406 and that produced by the *Pinnacle*³ inverse planning algorithm are shown in Figure 4. All
 407 constraints of the less challenging dose objectives were met by the DVSF algorithm (Algo-
 408 rithm 5) whereas *Pinnacle*³ exceeded the maximum dose for the OAR and did not satisfy
 409 the PTV minimum dose constraint. It should be noted that the *Pinnacle*³ inverse planning

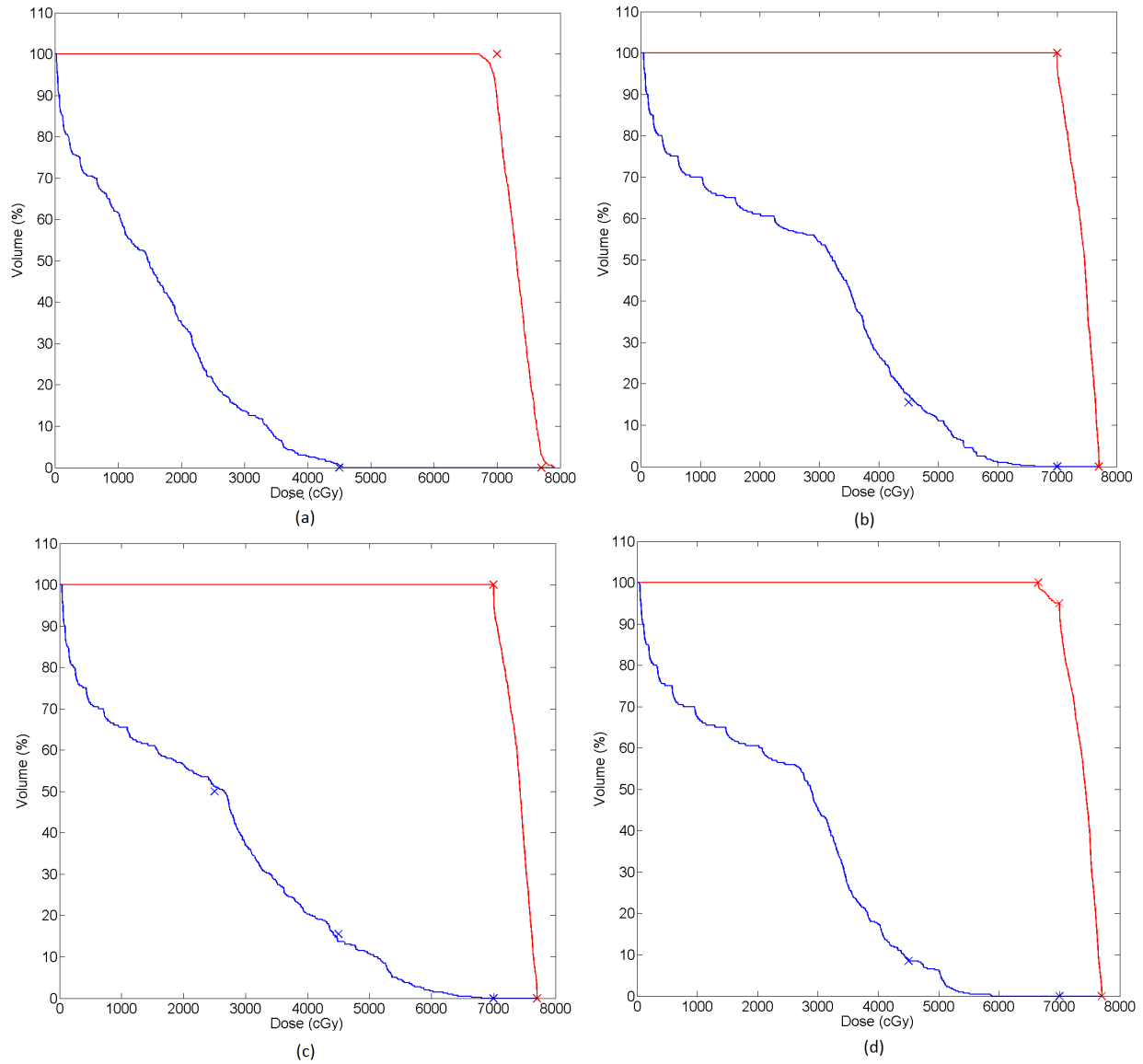


Figure 3: Dose-volume histograms for each of the prescriptions tested in the 2D C-shaped geometry. (a) Prescription 1 (b) Prescription 2 (c) Prescription 3 (d) Prescription 4. Red lines correspond to the PTV and blue lines to the OAR. Crosses indicate the DVCs.

410 was run only once with unit weighting on all dose objectives. It is possible that alteration
 411 of the objective weightings by trial-and-error may have resulted in a more desirable dose
 412 distribution. However, the objective of the current work was to compare the inherent ability
 413 of the algorithms to satisfy the inverse problem, and as such, iterative plan refinement by
 414 altering objective weights was not considered. Dose distributions for Prescription 1 of Table
 415 2 are shown in a single axial slice in Figure 5. The DVSF algorithm (Algorithm 5) showed
 416 higher conformality of the target structure.

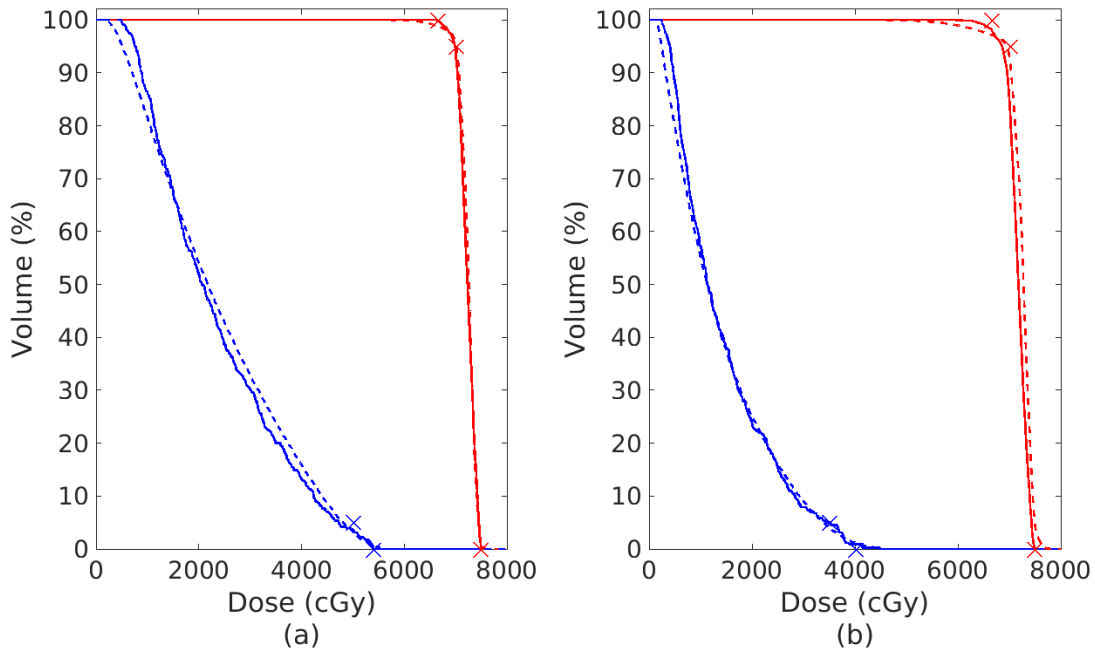


Figure 4: (a) Prescription 1 of Table 2: DVH after 2000 cycles of the DVSF algorithm (Algorithm 5) (solid), using $\gamma_{\text{PTV}} = 1.99/\theta_{\text{PTV}}$, $\gamma_{\text{OAR}} = 1/\theta_{\text{OAR}}$, $\lambda_{\text{PTV}} = \lambda_{\text{OAR}} = 1$, compared to the DVH produced by *Pinnacle*³ (dashed) after 86 iterations and meeting a stopping tolerance of less than 10^{-7} . (b) Prescription 2 of Table 2: DVH after 2000 cycles of the DVSF algorithm (Algorithm 5) (solid), using $\gamma_{\text{PTV}} = 1.99/\theta_{\text{PTV}}$, $\gamma_{\text{OAR}} = 0.3/\theta_{\text{OAR}}$, $\lambda_{\text{PTV}} = \lambda_{\text{OAR}} = 0.5$, compared to the DVH produced by *Pinnacle*³ (dashed) after 131 iterations and meeting a stopping tolerance of less than 10^{-7} .

417 Cumulative DVHs for Prescription 2 of Table 2 are shown in Figure 4(b). It is clear that
 418 both the DVSF algorithm (Algorithm 5) and *Pinnacle*³ had more difficulty meeting the dose
 419 objectives in this case. The DVSF algorithm (Algorithm 5) was better able to meet the

420 hard dose constraints when compared to *Pinnacle*³ but the latter was closer to meeting the
421 $D_{95} \geq 70$ Gy DVC on the PTV. Dose distributions for Prescription 2 of Table 2 are shown in
422 a single axial slice in Figure 6. Both dose distributions show cold spots in the target region.

423 4 Discussion and Conclusion

424 A new DVSF algorithm (Algorithm 5) based on feasibility-seeking has been successfully
425 applied to IMPT inverse planning in the current work. The proposed DVSF algorithm
426 (Algorithm 5) is based on a modification of the *CQ*-algorithm of Byrne [22] and is capable of
427 directly incorporating the DVCs associated with radiation therapy prescriptions into the split
428 feasibility-seeking problem statement. Our DVSF algorithm (Algorithm 5) is not restricted
429 to IMPT and is equally applicable to other forms of IMRT inverse planning. Test cases
430 consisted of a simplified 2D C-shape target surrounding an avoidance structure and a clinical
431 base of skull chordoma abutting the brainstem.

432 The DVSF algorithm (Algorithm 5) performs orthogonal projections to satisfy both the
433 DVCs and the lower and upper dose constraints. The AMS cyclic projection method [28] was
434 implemented for single-sided inequality dose objectives and the ARM algorithm of [23] was
435 implemented for interval inequalities (i.e., upper and lower dose bounds for a given structure).

436 A series of experiments were performed with 2D C-shaped geometry using varying DVCs
437 to validate the functionality of our DVSF algorithm (Algorithm 5). While DVC aims were
438 not met in all cases within the allowed number of iterations, the shape of the DVH curve
439 verified that the algorithm was attempting to meet these objectives. Experimentation with
440 user-defined relaxation parameter values γ and λ was performed to investigate the effect of
441 these settings on algorithmic performance. When λ was left at the fixed value of 1, it was
442 found that γ values closer to the upper allowable limit of $2/\theta$ were required to meet the DVC
443 aims. Further work concerning automatic choice of these user-defined parameters is currently
444 being undertaken and will be presented in future investigations.

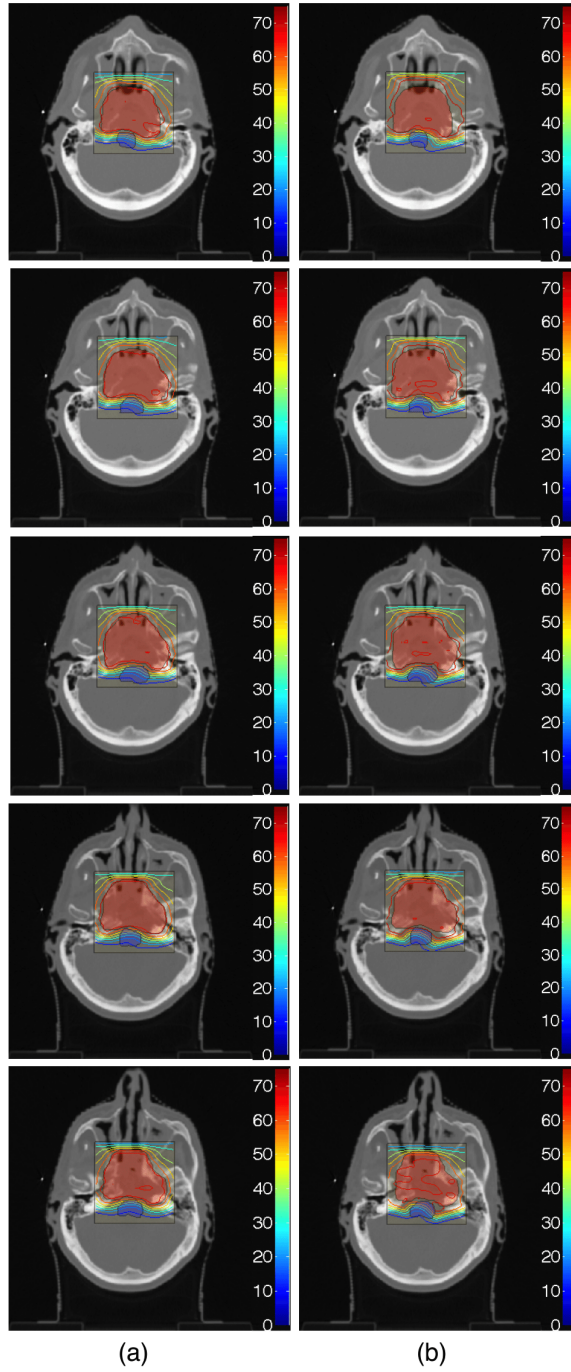


Figure 5: Dose contour map for Prescription 1 of Table 2 (a) after 2000 cycles of the DVSF algorithm (Algorithm 5), using $\gamma_{\text{PTV}} = 1.99/\theta_{\text{PTV}}$, $\gamma_{\text{OAR}} = 1/\theta_{\text{OAR}}$, $\lambda_{\text{PTV}} = \lambda_{\text{OAR}} = 1$, compared to (b) the dose contour map produced by *Pinnacle*³ after 86 iterations and meeting a stopping tolerance of less than 10^{-7} . The red shaded area is the PTV and the blue shaded area is the OAR (brainstem). Colour bar has units of Gy.

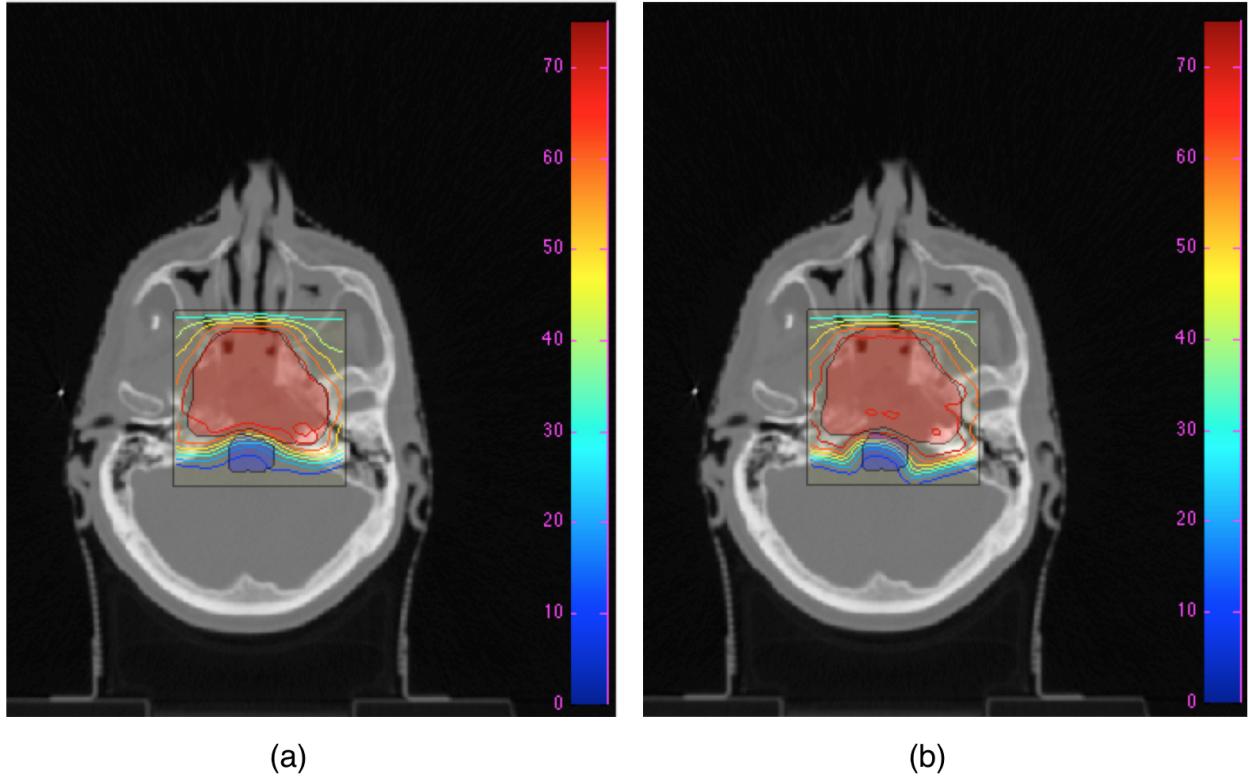


Figure 6: Dose contour map for Prescription 2 of Table 2 (a) after 2000 cycles of the DVSF algorithm (Algorithm 5), using $\gamma_{\text{PTV}} = 1.99/\theta_{\text{PTV}}$, $\gamma_{\text{OAR}} = 0.3/\theta_{\text{OAR}}$, $\lambda_{\text{PTV}} = \lambda_{\text{OAR}} = 0.5$, compared to (b) dose contour maps produced by *Pinnacle*³ after 131 iterations and meeting a stopping tolerance of less than 10^{-7} . The red shaded area is the PTV and the blue shaded area is the OAR (brainstem). Colour bar has units of Gy.

445 A clinical 3D IMPT treatment geometry was also investigated. The performance of the
446 DVSF algorithm (Algorithm 5) was compared to that of the research release of *Pinnacle*³
447 with proton pencil beam scanning. The shape of DVHs differed for the two inverse planning
448 algorithms. For the prescriptions investigated, our DVSF algorithm (Algorithm 5) was found
449 to result in a more conformal dose distribution when assessing isodose contours and DVH
450 distributions. It is acknowledged that the dose distributions obtained with *Pinnacle*³ may
451 be improved with the addition of planning structures. However, to allow for a comparison of
452 the inverse planning algorithms directly, no such structures were included in the treatment
453 planning method.

454 While the implementation of the DVSF algorithm (Algorithm 5) was sequential in the
455 current work, the structure of the algorithm lends itself to parallelization. For example,
456 block-iterative or string-averaging projection operators may be used when performing the
457 orthogonal projections described in Step 3 of Algorithm 5. Such implementations will not
458 only have benefits in computational speed, but may also result in superior dose distributions,
459 as has been observed in the use of these algorithms in tomographic image reconstruction [37].
460 Further work will examine the potential of block-iterative and string-averaging algorithmic
461 schemes for the DVSF algorithm (Algorithm 5).

462 5 Appendix

463 Here is a proof of formula (22) for the projection calculation onto the non-convex set Q .

464 **Proof.** We show that the following translation formula

$$P_Q(z) = P_{\bar{Q}}(z - b^1) + b^1 \tag{36}$$

465 holds true for every $z \in R^{m_1}$, despite the fact that P_Q and $P_{\overline{Q}}$ are set-valued, i.e., a point
 466 $z \in R^{m_1}$ might have more than one projection onto the set. Note that

$$\overline{Q} = Q - b^1. \quad (37)$$

467 By the definition of projection of a point onto a set,

$$q_0 \in P_Q(z) \text{ if and only if } q_0 \in Q \text{ and } \|z - q_0\| \leq \|z - q\|, \text{ for all } q \in Q. \quad (38)$$

468 Similarly, $(q_0 - b^1) \in P_{\overline{Q}}(z - b^1)$ if and only if $(q_0 - b^1) \in \hat{Q}$ and

$$\|(z - b^1) - (q_0 - b^1)\| \leq \|(z - b^1) - \bar{q}\| \quad (39)$$

holds for every $\bar{q} \in \overline{Q}$. Therefore, by (37), (38) and (39), we have the following equivalences

$$\begin{aligned} q_0 \in P_Q(z) &\iff q_0 \in Q \text{ and } \forall_{q \in Q} \|z - q_0\| \leq \|z - q\| \\ &\iff (q_0 - b^1) \in \overline{Q} \text{ and} \\ &\forall_{q \in Q} \|(z - b^1) - (q_0 - b^1)\| \leq \|(z - b^1) - (q - b^1)\| \\ &\iff (q_0 - b^1) \in \overline{Q} \text{ and} \\ &\forall_{\bar{q} \in \overline{Q}} \|(z - b^1) - (q_0 - b^1)\| \leq \|(z - b^1) - \bar{q}\| \\ &\iff (q_0 - b^1) \in P_{\overline{Q}}(z - b^1) \\ &\iff q_0 \in P_{\overline{Q}}(z - b^1) + b^1, \end{aligned} \quad (40)$$

469 which completes the proof. ■

470 **Acknowledgments.** We thank the two anonymous referees for their constructive com-
 471 ments which helped us improve the paper. The work of Y. Censor and R. Schulte was
 472 supported by Research Grant No. 2013003 of the United States-Israel Binational Science
 473 Foundation (BSF) and by Award No. 1P20183640-01A1 of the National Cancer Institute

474 (NCI) of the National Institutes of Health (NIH). The authors thank *Philips* for technical
475 assistance with *Pinnacle*³ software for this research.

476 **References**

- 477 [1] C. E. Coles, A. M. Moody, C. B. Wilson, and N. G. Burnet, “Reduction of radiotherapy-
478 induced late complications in early breast cancer: the role of intensity-modulated ra-
479 diation therapy and partial breast irradiation: Part I - normal tissue complications,”
480 *Clinical Oncology*, vol. 17, pp. 16–24, 2005.
- 481 [2] R. Mohan, Q. Wu, M. Manning, and R. Schmidt-Ullrich, “Radiobiological considerations
482 in the design of fractionation strategies for intensity-modulated radiation therapy of head
483 and neck cancers,” *International Journal of Radiation Oncology • Biology • Physics*,
484 vol. 46, pp. 619–630, 2000.
- 485 [3] A. Narayana, J. Yamada, S. Berry, P. Shah, M. Hunt, P. H. Gutin, and S. A. Leibel,
486 “Intensity-modulated radiotherapy in high-grade gliomas: Clinical and dosimetric re-
487 sults,” *International Journal of Radiation Oncology • Biology • Physics*, vol. 64, pp. 892–
488 897, 2006.
- 489 [4] C. M. Nutting, D. J. Convery, V. P. Cosgrove, C. Rowbottom, A. R. Padhani, S. Webb,
490 and D. P. Dearnaley, “Reduction of small and large bowel irradiation using an optimized
491 intensity-modulated pelvic radiotherapy technique in patients with prostate cancer,”
492 *International Journal of Radiation Oncology • Biology • Physics*, vol. 48, pp. 649–656,
493 2000.
- 494 [5] S. Sura, V. Gupta, E. Yorke, A. Jackson, H. Amols, and K. E. Rosenzweig, “Intensity-
495 modulated radiation therapy (IMRT) for inoperable non-small cell lung cancer: The
496 Memorial Sloan-Kettering Cancer center (MSKCC) experience,” *Radiotherapy and On-
497 cology*, vol. 87, pp. 17–23, 2008.

- 498 [6] A. J. Lomax, E. Pedroni, H. P. Rutz, and G. Goitein, “The clinical potential of intensity
499 modulated proton therapy,” *Zeitschrift für Medizinische Physik*, vol. 14, pp. 147–152,
500 2004.
- 501 [7] H. M. Kooy and C. Grassberger, “Intensity modulated proton therapy,” *British Journal*
502 *of Radiology*, vol. 88, p. 20150195, 2015.
- 503 [8] L. V. van Dijk, R. J. H. M. Steenbakkers, B. ten Haken, H. P. van der Laan, A. A.
504 van’t Veld, J. A. Langendijk, and E. W. Korevaar, “Robust intensity modulated proton
505 therapy (IMPT) increases estimated clinical benefit in head and neck cancer patients,”
506 *PLoS ONE*, vol. 11, pp. 1–14, 2016.
- 507 [9] J. Welsh, D. Gomez, M. B. Palmer, B. A. Riley, A. V. Mayankkumar, R. Komaki,
508 L. Dong, X. R. Zhu, A. Likhacheva, Z. Liao, W. L. Hofstetter, J. A. Ajani, and J. D.
509 Cox, “Intensity-modulated proton therapy further reduces normal tissue exposure during
510 definitive therapy for locally advanced distal esophageal tumors: A dosimetric study,”
511 *International Journal of Radiation Oncology • Biology • Physics*, vol. 81, pp. 1336–1342,
512 2011.
- 513 [10] X. Zhang, Y. Li, X. Pan, L. Xiaoqiang, R. Mohan, R. Komaki, J. D. Cox, and J. Y.
514 Chang, “Intensity-modulated proton therapy reduces the dose to normal tissue compared
515 with intensity-modulated radiation therapy or passive scattering proton therapy and
516 enables individualized radical radiotherapy for extensive stage IIIB non-small-cell lung
517 cancer: A virtual clinical study,” *International Journal of Radiation Oncology • Biology*
518 *• Physics*, vol. 77, pp. 357–366, 2010.
- 519 [11] S. L. Gulliford, K. Foo, R. C. Morgan, E. G. Aird, A. M. Bidmead, H. Critchley, P. M.
520 Evans, S. Gianolini, W. P. Mayles, A. R. Moore, B. Sanchez-Nieto, M. Partridge, M. R.
521 Sydes, S. Webb, and D. P. Dearnaley, “Dose-volume constraints to reduce rectal side
522 effects from prostate radiotherapy: Evidence from MRC RT01 trial ISRCTN 47772397,”

- 523 *International Journal of Radiation Oncology • Biology • Physics*, vol. 76, pp. 747–754,
524 2010.
- 525 [12] “The radiation therapy oncology group (RTOG) 1308 protocol: Phase III randomized
526 trial comparing overall survival after photon versus proton chemoradiotherapy for in-
527 operable stage II-IIIB NSCLC.” Current Version Date: October 5, 2015, Available at:
528 <https://www.rtog.org/ClinicalTrials/ProtocolTable/StudyDetails.aspx?study=1308>.
- 529 [13] S. V. Spirou and C. S. Chui, “A gradient inverse planning algorithm with dose-volume
530 constraints,” *Medical Physics*, vol. 25, pp. 321–333, 1998.
- 531 [14] P. S. Cho, S. Lee, R. J. Marks II, S. Oh, S. G. Sutlief, and M. H. Phillips, “Optimization
532 of intensity modulated beams with volume constraints using two methods: cost function
533 minimization and projections onto convex sets,” *Medical Physics*, vol. 25, pp. 435–443,
534 1998.
- 535 [15] H. E. Romeijn, R. K. Ahuja, J. F. Dempsey, A. Kumar, and J. G. Li, “A novel linear
536 programming approach to fluence map optimization for intensity modulated radiation
537 therapy treatment planning,” *Physics in Medicine and Biology*, vol. 48, pp. 3521–3542,
538 2003.
- 539 [16] H. E. Romeijn, R. K. Ahuja, J. F. Dempsey, and A. Kumar, “A new linear program-
540 ming approach to radiation therapy treatment planning problems,” *Operations Research*,
541 vol. 54, pp. 201–216, 2006.
- 542 [17] Y. Zhang and M. Merritt, “Dose-volume-based IMRT fluence optimization: A fast least-
543 squares approach with differentiability,” *Linear Algebra and its Applications*, vol. 428,
544 pp. 1365–1387, 2008.
- 545 [18] H. H. Bauschke and J. M. Borwein, “On projection algorithms for solving convex feasi-
546 bility problems,” *SIAM Review*, vol. 38, pp. 367–426, 1996.

- 547 [19] Y. Censor and A. Cegielski, “Projection methods: An annotated bibliography of books
548 and reviews,” *Optimization*, vol. 64, pp. 2343–2358, 2015.
- 549 [20] Y. Censor, W. Chen, P. Combettes, R. Davidi, and G. Herman, “On the effectiveness of
550 projection methods for convex feasibility problems with linear inequality constraints,”
551 *Computational Optimization and Applications*, vol. 51, pp. 1065–1088, 2011.
- 552 [21] S. Penfold, M. Casiraghi, T. Dou, R. Schulte, and Y. Censor, “A feasibility-seeking al-
553 gorithm applied to planning of intensity modulated proton therapy: A proof of principle
554 study,” *Medical Physics*, vol. 42, p. 3338, 2015.
- 555 [22] C. Byrne, “Iterative oblique projection onto convex sets and the split feasibility prob-
556 lem,” *Inverse Problems*, vol. 18, pp. 441–453, 2002.
- 557 [23] Y. Censor, “An automatic relaxation method for solving interval linear inequalities,”
558 *Journal of Mathematical Analysis and Applications*, vol. 106, pp. 19–25, 1985.
- 559 [24] Y. Censor, M. D. Altschuler, and W. D. Powlis, “A computational solution of the inverse
560 problem in radiation-therapy treatment planning,” *Applied Mathematics and Computa-
561 tion*, vol. 25, pp. 57–87, 1988.
- 562 [25] Y. Censor, A. Ben-Israel, Y. Xiao, and J. M. Galvin, “On linear infeasibility arising in
563 intensity-modulated radiation therapy inverse planning,” *Linear Algebra and its Appli-
564 cations*, vol. 428, pp. 1406–1420, 2008.
- 565 [26] Y. Censor, “Mathematical optimization for the inverse problem of intensity-modulated
566 radiation therapy,” in *Intensity-Modulated Radiation Therapy: The State of The Art*,
567 *American Association of Physicists in Medicine, Medical Physics Monograph No. 29*
568 (J. R. Palta and T. R. Mackie, eds.), pp. 25–49, Medical Physics Publishing, Madison,
569 Wisconsin, USA, 2003.
- 570 [27] A. Cegielski, *Iterative Methods for Fixed Point Problems in Hilbert Spaces, Lecture Notes
571 in Mathematics*, vol. 2057. Springer-Verlag, Berlin, Heidelberg, Germany, 2012.

- 572 [28] S. Agmon, “The relaxation method for linear inequalities,” *Canadian Journal of Math-*
573 *ematics*, vol. 6, pp. 382–392, 1954.
- 574 [29] T. S. Motzkin and I. J. Schoenberg, “The relaxation method for linear inequalities,”
575 *Canadian Journal of Mathematics*, vol. 6, pp. 393–404, 1954.
- 576 [30] G. T. Herman, “A relaxation method for reconstructing objects from noisy x-rays,”
577 *Mathematical Programming*, vol. 8, pp. 1–19, 1975.
- 578 [31] Y. Censor and S. A. Zenios, *Parallel Optimization: Theory, Algorithms, and Applica-*
579 *tions*. Oxford University Press, New York, NY, USA, 1997.
- 580 [32] Y. Censor and T. Elfving, “A multiprojection algorithm using Bregman projections in
581 a product space,” *Numerical Algorithms*, vol. 8, pp. 221–239, 1994.
- 582 [33] Y. Censor, T. Elfving, N. Kopf, and T. Bortfeld, “The multiple-sets split feasibility
583 problem and its applications for inverse problems,” *Inverse Problems*, vol. 21, pp. 2071–
584 2084, 2005.
- 585 [34] Y. Censor, A. Gibali, and S. Reich, “Algorithms for the split variational inequality
586 problem,” *Numerical Algorithms*, vol. 59, pp. 301–323, 2012.
- 587 [35] C. Byrne, “Bounds on the largest singular value of a matrix and the convergence of
588 simultaneous and block-iterative algorithms for sparse linear systems,” *International*
589 *Transactions in Operational Research*, vol. 16, pp. 465–479, 2009.
- 590 [36] S. Agostinelli *et al.*, “Geant4—a simulation toolkit,” *Nuclear Instruments and Methods*
591 *in Physics Research Section A: Accelerators, Spectrometers, Detectors and Associated*
592 *Equipment*, vol. 506, pp. 250–303, 2003.
- 593 [37] S. N. Penfold, R. W. Schulte, Y. Censor, V. Bashkirov, S. McAllister, K. E. Schubert, and
594 A. B. Rosenfeld, “Block-iterative and string-averaging projection algorithms in proton
595 computed tomography image reconstruction,” in *Biomedical Mathematics: Promising*

596

Directions in Imaging, Therapy Planning and Inverse Problems (Y. Censor, M. Jiang,

597

and G. Wang, eds.), pp. 347–367, Medical Physics Publishing, Madison, WI, USA, 2010.